ESC-TR-2007-082

Technical Report
1141

RF Radiation Environment Over Millstone Hill

T.A. Cott

14 December 2009

Lincoln Laboratory
MASSACHUSETTS INSTITUTE OF TECHNOLOGY
LEXINGTON, MASSACHUSETTS

Prepared for the Department of the Air Force under Contract FA8721-05-C-0002.

This report is based on studies performed at Lincoln Laboratory, a center for research operated by Massachusetts Institute of Technology. This work was sponsored by the Department of the Air Force, 850 ELSG/NSS, under Contract FA8721-05-C-0002.

The 66ABW Public Affairs Office has reviewed this report, and it is releasable to the National Technical Information Service, where it will be available to the general public, including foreign nationals.

This technical report has been reviewed and is approved for publication.

FOR THE COMMANDER

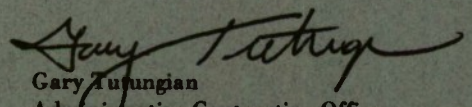

Gary Tutungian
Administrative Contracting Officer
Plans and Programs Directorate
Contracted Support Management

Massachusetts Institute of Technology
Lincoln Laboratory

RF Radiation Environment Over Millstone Hill

T.A. Cott
Group 93

Technical Report 1141

14 December 2009

Lexington Massachusetts

This page intentionally left blank.

ABSTRACT

This report documents a study of the RF radiation environment in the vicinity of the Lincoln Space Surveillance Complex radars. The focus of ti HOPEhe study is a model-based analysis of the hazards to occupants of aircraft flying in the vicinity of the radars, comparing computed exposure levels with safety standards for the general public set by the Massachusetts Department of Public Health.

This page intentionally left blank.

ACKNOWLEDGMENTS

Bob Norander of Group 92 at Millstone helped a great deal in gathering much of the information for this analysis as well as offering suggestions for this report, as did Eric Phelps and Gary Krumpholz of Group 92. Thanks also go to Steve Campbell, Bill Harman, Mel Stone, and others in Group 42, Air Traffic Control Systems, for reviewing the report and advising on flight patterns and conditions in the vicinity of the Lincoln Space Surveillance Complex.

This page intentionally left blank.

TABLE OF CONTENTS

This page intentionally left blank.

LIST OF ILLUSTRATIONS

LIST OF ILLUSTRATIONS (Continued)

LIST OF TABLES

This page intentionally left blank.

1. INTRODUCTION

In 2001, Millstone Hill staff reeeived a eommunieation from a flight instruetor based at a nearby airport (Nashua, New Hampshire), eoncerning the safety of flying near the radars loeated at the Lineoln Spaee Surveillanee Complex (LSSC). Indeed, when the weather is good, single-engine aireraft ean often be seen flying over the LSSC radars, using the site as a eonvenient and interesting visual waypoint. Presented below are the estimated eleetromagnetie field strengths these aireraft, flying in proximity to the radar systems, may be exposed to, as are eomparisons of the results to exposure limits established for the general publie by the Massaehusetts Department of Publie Health. In 2009, this report was updated to inelude the planned Haystaek Ultrawideband Satellite Imaging Radar (HUSIR).

The risk of radio frequency (RF) radiation exposure is small. The LSSC radars operate on limited sehedules; 65 to 80 hours per week, often in the evening and overnight hours. In addition, the radar systems all employ peneil-beams whose half-power widths range from the 1° MISA UHF to the 0.06° Haystack LRIR and 0.006° for the planned HUSIR. Finally, for all the radars, an aireraft must stay in the peneil-beam for many seeonds at relatively elose range before it experienees signifieant exposure levels. It is also reasonable to expeet that the strueture of an aireraft will offer some degree of shielding for the oeeupants to ineident eleetromagnetie waves, though the extent of this effeet is very difficult to quantify. It is important to note that the results presented herein assume no sueh shielding effeet.

This report does not attempt to evaluate the overall risk to oeeupants of aireraft flying over the site, but instead studies fixed-wing aireraft beam-erossing and helieopter in-beam dwell seenarios and presents the eomputed exposure level results for the Millstone, Haystaek, HUSIR, HAX, MISA, and Zenith radars. The fixed-wing aireraft flight geometries analyzed are nearly worst-ease, presuming a fixed heading in level flight and ground speeds near a single-engine aireraft stall speed. The radar state is also nearly worst-ease, presuming fixed angle pointing at fairly low elevation for the duration of the eneounter. The fixed-wing results presented below, therefore, should be eonsidered to have low probabilities of oeeurrenee. These results indieate that, even under these eireumstanees, aireraft are not exposed to RF radiation beyond state established limits. The same methodology is also applied to estimate the exposure levels for birds flying through the radar beam. The eoneern about potential hazards to birds eame up in eonnection with the HUSIR program.

Worst-ease helieopter dwell seenarios are presented for a hover within one dish radius of antenna boresight and at elose range. Unlike the fixed-wing eneounter deseribed above, this seenario is quite possible for the Millstone, MISA, and Zenith radars given the interesting nature of peering into a large antenna aperture (the Haystaek and HAX radars are eovered by radomes, as will be HUSIR). Results for this ease indieate a potential for a signifieant RF radiation hazard if aireraft eome too elose to the radar while it is in operation.

This analysis is intended to faeilitate the speeifieation of a Federal Aviation Administration Notiee to Airmen (NOTAM) speeifying a zone eentered on the LSSC alerting pilots to the RF environment there.

This page intentionally left blank.

2. METHODOLOGY

There are innumerable scenarios that describe how an aircraft might interact with the beam of a radiating antenna of circular aperture. In the case of fixed-wing aircraft, many involve the aircraft circling the site and, so, transiting the radar beam in a very short period of time (if the aircraft encounters the beam at all). The worst-case situation, where an aircraft in flight can stay within the beam for an extended period, involves the aircraft in level flight on a fixed heading, and the radar pointing also fixed and at a low elevation angle. The resulting angle of the flight-path with respect to the radar line of sight (RLOS) is small and the exposure time of the aircraft is increased. Figure 1 illustrates this scenario. Computation of exposure levels for this scenario is performed by computing field strength along the flight path and adjusting it for the transit time of the aircraft. With an appropriate choice of air speed, the same methodology can be applied to estimate exposure levels for birds flying through the radar beam.

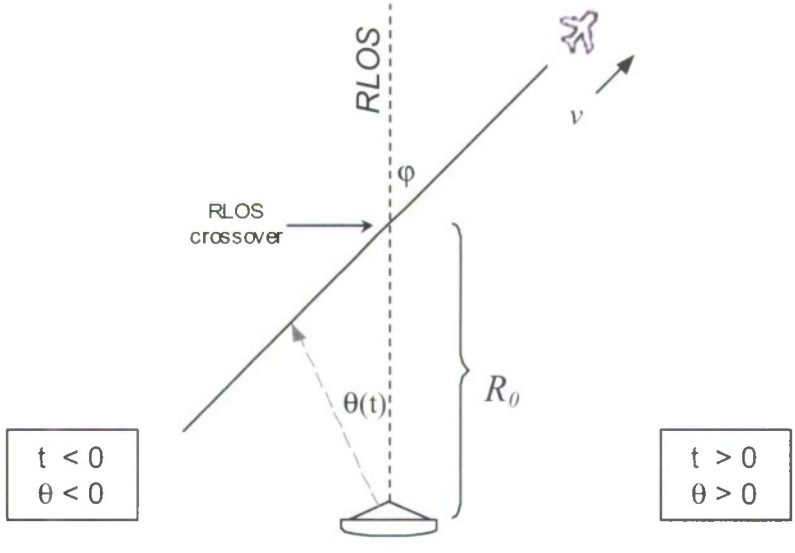

Figure 1. Aircraft beam-crossing scenario. Aircraft flies with a groundspeed of v and a heading at an angle φ with respect to the radar line-of-sight (RLOS). The flight path intersects the RLOS at a range of R_0 from the antenna. The vector to the aircraft has an angle θ(t) w.r.t. the RLOS.

Scenarios involving a helicopter interacting with a radar beam are also innumerable, with the worst case being a helicopter in a hover within the beam of the antenna at close range. In this case, field strength is computed at a fixed position and scaled based on the dwell time.

Computation of the final average field power flux for comparison to established limits is described in the following sections for both far-field and near-field models. The regions of applicability of far-field and near-field assumptions are frequently a source of uncertainty (particularly in this situation where direct measurement of the fields is not possible) so both are evaluated. Under the far-field assumption, the flux is computed as a function of range, the beam transit time of the aircraft is determined, and the result

is scaled by the antenna beam pattern. Under the near-field assumption, the normalized field strength is computed as a function of range and angle and is scaled by the field strength in the antenna aperture for the final result. Both are then scaled for an equivalent 30-minute average, based on the time in the beam, for comparison to established standards.

2.1 FIXED-WING SCENARIO GEOMETRY

There are two phases of the beam transit, the in-range portion and the out-range portion, with the time of RLOS crossover defined as $t = 0$. The in-range portion (inside of the RLOS crossover point) is negative time (t) and negative angle (θ), as depicted in Figure 1.

The angle between the aircraft and the RLOS as viewed from the radar, $\theta(t)$, is

$$\theta(t) = \tan^{-1}\left[\frac{vt\sin\varphi}{R_0 + vt\cos\varphi}\right] \text{ (rad)}, \tag{1}$$

where

v – aircraft ground speed (m/s)
t – time from RLOS crossover (sec)
φ – angle between flight path and RLOS (rad)
R_0 – range to RLOS crossover (m)

The time derivative (helpful in quick approximations, but not used here) is

$$\frac{d}{dt}\theta(t) = \frac{R_0 v\sin\varphi}{R_0^2 + 2R_0 vt\cos\varphi + (vt)^2} \text{ (rad/s)}. \tag{2}$$

Solving $\theta(t)$ for t,

$$t(\theta) = \frac{R_0}{\dfrac{v\sin\varphi}{\tan\theta} - v\cos\varphi} \text{ (sec)}, \tag{3}$$

which can be evaluated at the two beam edges to determine the transit times. The range to the aircraft, expressed as a function of time, is

$$R(t) = \left[R_0^2 + 2R_0 vt\cos\varphi + (vt)^2\right]^{1/2} \text{ (m)}. \tag{4}$$

2.2 BEAM PATTERN APPROXIMATION

A generous approximation has been made of the angle response of the radiating antenna. A triangular response is used for the one-way power as a function of angle from boresight, whose peak is at $\theta = 0°$ and whose base runs between the first sidelobes of the pattern (see Figure 2).

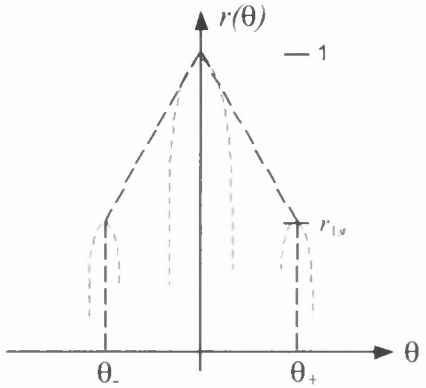

Figure 2. Pattern approximation is a triangular response on a pedestal at the first sidelobes. The angular positions of the first sidelobes are denoted θ_- and θ_+.

The beam pattern factor, the average response power of the antenna over the beam size (defined as the range of angle between the first pattern sidelobes), is

$$F_{beam} = 0.5(1 + r_{1st}) , \tag{5}$$

where r_{1st} is the normalized one-way response power of the first sidelobe.

Typically, well-illuminated large circular antenna apertures will have sidelobes more than 15 dB below (0.032) the boresight response, yielding beam factors near 0.5. A numerical integration of the measured Millstone Hill Radar antenna pattern yields an average response power of 0.31 between the first sidelobes and 0.43 over the main lobe.

2.3 FAR-FIELD POWER FLUX

The shorter the range to the radar line-of-sight (RLOS) crossover, the higher the field strength experienced by the aircraft. At a far-field range R, the peak field power flux experienced on a single pulse is

$$S_{peak}(R) = \frac{P_X G_X}{4\pi R^2} \frac{1}{L_X} \text{ (W/m}^2\text{)} , \tag{6}$$

where

P_X – peak transmit power (W)
G_X – antenna transmit gain
R – range to aircraft (m)
L_X – transmit system losses

or, incorporating system constants,

$$S_{peak}(R) = \frac{K}{R^2} \ (\mathrm{W/m^2}) . \tag{7}$$

The average field power flux, accounting for the duty cycle (D) of the pulsed radar signal, is

$$S_{ave}(R) = S_{peak}(R) \cdot D \ (\mathrm{W/m^2}) . \tag{8}$$

Substituting for R in (7) with $R(t)$ from (4) gives

$$S_{peak}(t) = \frac{K}{R_0^2 + 2R_0 vt\cos\varphi + (vt)^2} . \tag{9}$$

The average single-pulse power flux encountered by the aircraft during the beam transit time (excluding antenna pattern effects) is then

$$\begin{aligned} \overline{S_{peak}} &= \frac{1}{t_{\theta+} - t_{\theta-}} \int_{\theta-}^{\theta+} S_{peak}(t)dt \\ &= \frac{K}{R_0 v \sin\varphi (t_{\theta+} - t_{\theta-})} \tan^{-1}\left[\frac{vt + R_0\cos\varphi}{R_0 \sin\varphi}\right]_{t_{\theta-}}^{t_{\theta+}} , \end{aligned} \tag{10}$$

where $t_{\theta-}$ is the time at the in-range beam edge and $t_{\theta+}$ is the time at the out-range beam edge.

Finally, scaling by the duty cycle and beam pattern factors for the final average power flux yields

$$\overline{S_{ave}} = \overline{S_{peak}} \cdot D \cdot F_{beam} . \tag{11}$$

Alternately, the average power flux may be computed by numerically integrating the product of the peak power flux (S_{peak}) and the antenna pattern response (F_{ant}):

$$\overline{S_{ave}} = \frac{D}{t_{\theta+} - t_{\theta-}} \int_{\theta-}^{\theta+} S_{peak}[R(t)] \cdot F_{ant}[\theta(t)]dt . \tag{12}$$

This method was used to check the results from (11), which is a product of averages rather than an average of a product. A scan of the Millstone antenna pattern was used for $F_{ant}(\theta)$. Results using this method agree to two decimal places with those computed by the approximation in (11) using $F_{beam} = 0.31$, the average beam pattern factor between the first sidelobes.

2.4 NEAR-FIELD APPROXIMATION

Due to the relatively large apertures and short wavelengths of the LSSC radar systems, aircraft flying in the vicinity (out of curiosity or while using the antennas for visual reference) are often operating in the near-field of these systems. Typically, near-field issues are of interest on compact antenna ranges

where the peculiar effects can be measured directly. Measurements of this kind have shown that the field strength in front of a circular aperture antenna does not drop significantly with increased range [1], meaning the exposure levels encountered by aircraft near the LSSC are most likely higher than those predicted by the far-field model using a power decay rate of R^{-2}. Sufficiently thorough direct measurement of the near-fields of the LSSC radars is not possible, so a modeling approach is required.

A search of the literature shows that few analytic approximations for the near-field of large circular apertures have been offered in the past. One such approximation, by L.Z. Pazin [2], has been implemented, and the results are tabulated with the R^{-2} results below. A numerical approach offered by R.L. Lewis and A.C. Newell [3] has also been implemented to corroborate the Pazin results. Both methods are now described.

2.5 ANALYTIC NEAR-FIELD MODEL

Pazin computes the complex components of the near-field by solving Maxwell's equations with the help of the Hertz vector method. This approach relies on the axially symmetric, equiphase illumination of a circular aperture such as those of the LSSC radars. The coordinate system layout is shown in Figure 3.

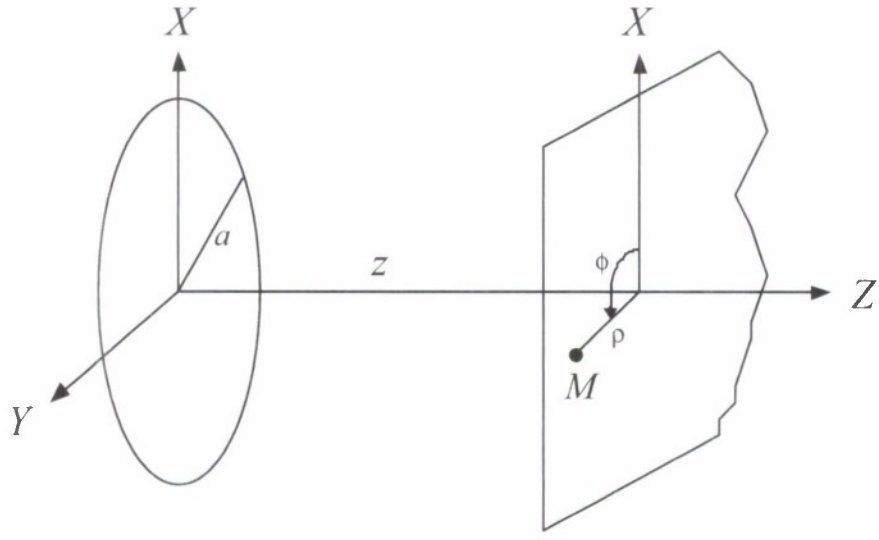

Figure 3. Pazin near-field model geometry. Electric field components are computed for point M in the observation plane parallel to, and distance z from, the antenna aperture of radius a. In the observation plane, M is distance ρ from the RLOS (z-axis) and angle φ from the x-axis.

Pazin computes the complex x-, y-, and z-components for a cartesian right-handed system whose x-y plane lies in the plane of the aperture and z-axis lies along the radar line-of-sight:

$$E_x = \left[\sum_{q=0}^{p} b_q \dot{W}_{1,2}(q,m,u) + \left(\frac{a}{z}\right)^2 \mu_x\right] \cdot je^{-j(kz+\psi_m)}$$

$$E_y = \left(\frac{a}{z}\right)^2 \mu_y \sin 2\varphi \cdot je^{-j(kz+\psi_m)} \qquad (13)$$

$$E_z = \left(\frac{a}{z}\right) \mu_z \cos\varphi \cdot je^{-j(kz+\psi_m)}$$

where

$$f(t) = \sum_{q=0}^{p} b_q t^{2q} \quad (p = 1,2, \ldots)$$

is the antenna illumination function ($f(t) = 1 - 1.5t^2 + 0.8t^4$ used; t is the normalized radial distance in the aperture). These components are normalized and are ultimately scaled by the field in the aperture of the transmitting antenna. Other parameters in (13) are now defined.

$$\dot{W}_{1,2}(q,m,u) = W_1(q,m,u) + jW_2(q,m,u)$$

are the special functions of three variables approximated by first-kind Bessel functions (orders 0, 1, and 2) and Lommel functions of two variables. The special function approximations are not shown here, but are included in the reference.

Other parameters are

$$m = ka^2/z$$

$$k = 2\pi/\lambda$$

$$\psi_m = \left(1+\tau^2\right)/2$$

$$\tau = \rho/a$$

$$u = k\rho a/z$$

and

$$\mu_x = \mu_y\left(1+2\cos^2\varphi\right)+ j\mu_z/u$$
$$\mu_y = -0.25 f(1)\left[\tau \cdot J_1(u) - jJ_2(u)\right]$$
$$\mu_z = -f(1)J_1(u)$$

where

$$f(1) = \sum_{q=0}^{p} b_q ,$$

with distances

- a – antenna aperture radius (m)
- z – distance along RLOS to plane parallel to aperture containing observation point (m)
- ρ – distance from RLOS to observation point in plane parallel to aperture (m)
- λ – wavelength (m)

The square of the near-field model output, normalized electric field strength, is scaled by the aperture power flux, which is known through the transmit power meters, the transmit losses between the meters and free space, and the antenna illumination function (i.e., taper). In fact, the free space impedance close to a complex antenna structure is not known, and so the actual energy balance between electric and magnetic fields at any given point close to the antenna is not known. For this reason, the near-field results presented below should be considered approximate indicators of radiation strength only.

Figure 4 shows a map of the E_x component amplitude over a region close to the antenna. The x-axis (m) is the scaled reciprocal of the distance from the aperture (the antenna is at the right), while the y-axis (τ) is the normalized distance from boresight (where 1.0 represents the aperture edge). As can be seen, numerous "hotspots" exist, with the most significant located at $m \cong 19$. The location of this hotspot for each of the LSSC radars is listed in Table 1. Also note the roll-off of field strength in the τ-direction; unlike the far-field case, the near-field beam remains well collimated with increasing range.

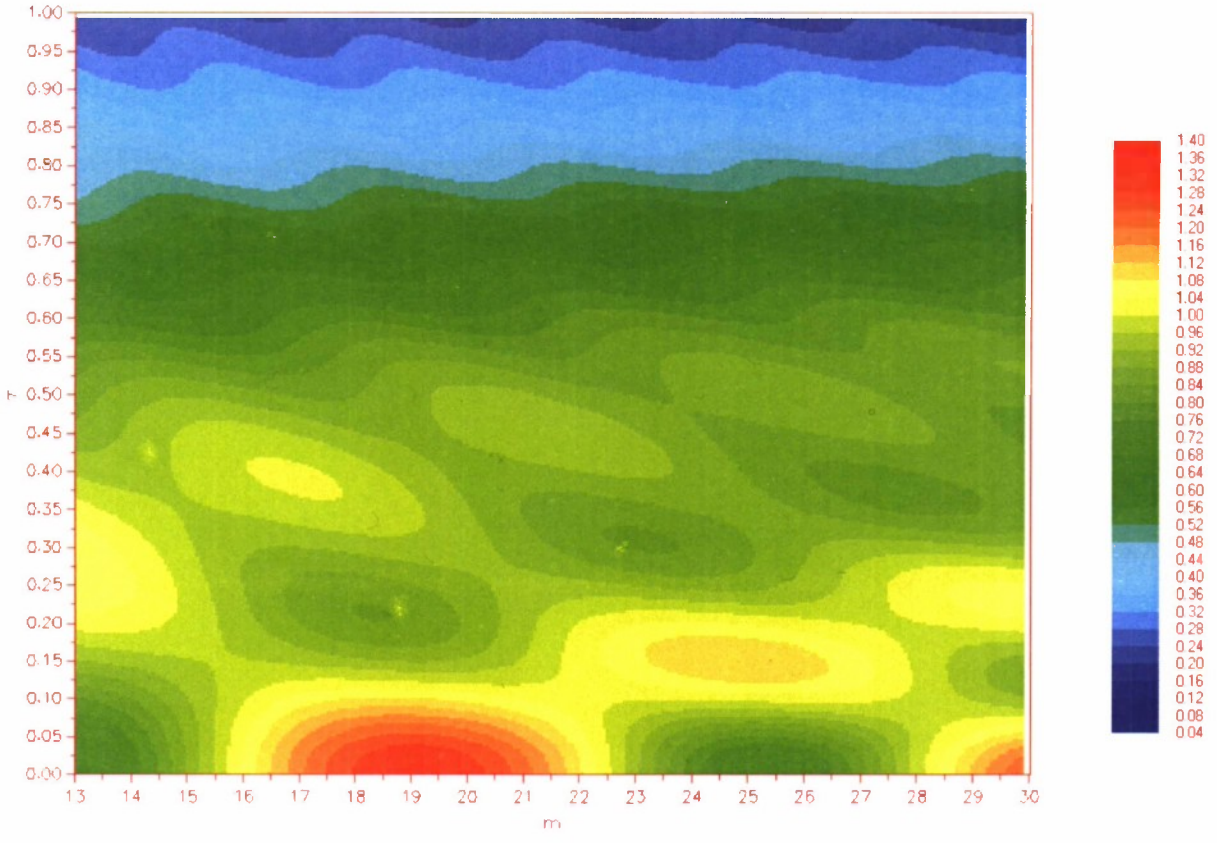

Figure 4. Near-field amplitude map. The x-axis (m) is inversely proportional to the distance from the aperture. Note the "hotspot" at m ≅ 19. The y-axis (τ) ranges from boresight (τ = 0) to the outer edge of the aperture (τ = 1).

Figure 5 shows the model field strength over the entire antenna aperture ($-1 \le \tau \le +1$) and out to half the distance to the traditional Fresnel-Fraunhofer boundary, defined

$$z_{FF} = \frac{2D^2}{\lambda}, \tag{14}$$

where D is the aperture diameter. This value is often used to define the boundary between the more complex near-field and simpler plane-wave far-field (R^{-2}) assumptions. The x-axis is parameterized as the distance fraction to z_{FF} ($\alpha = z/z_{FF}$), with the antenna now at the left.

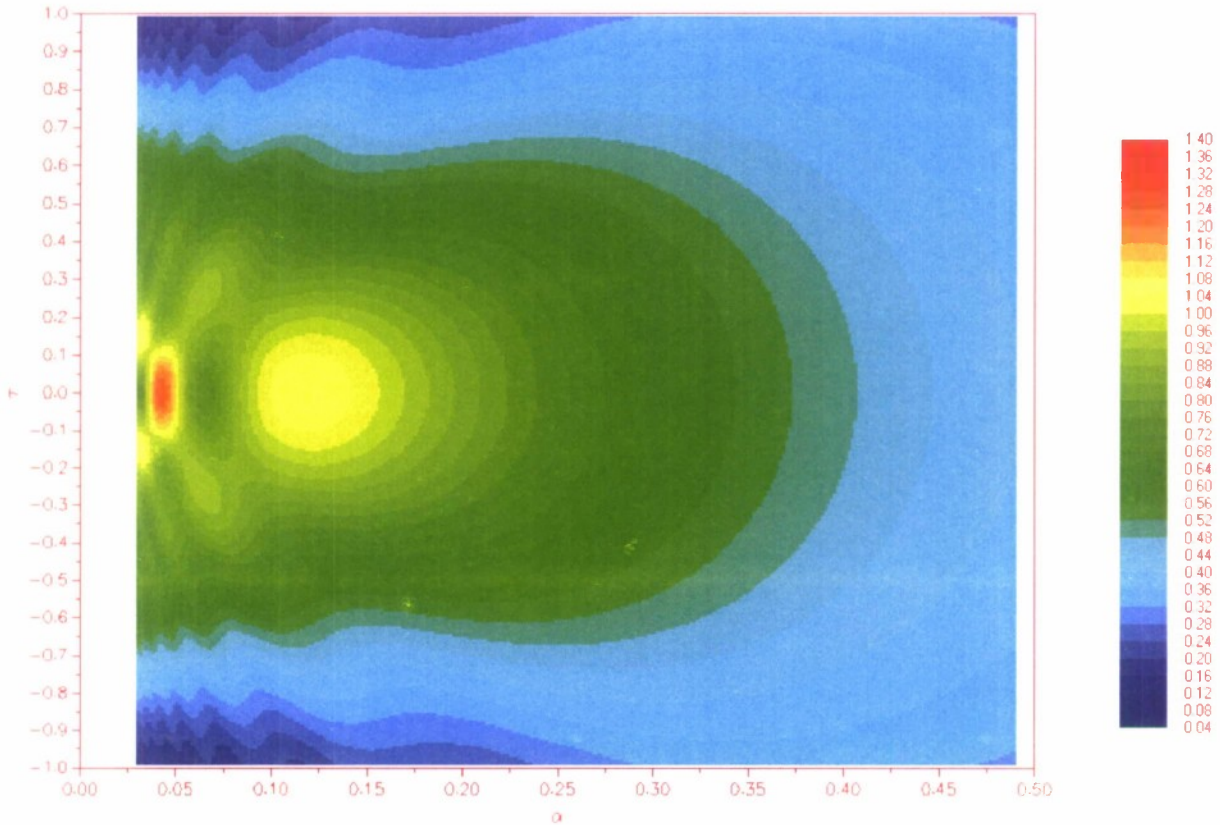

Figure 5. Near-field beam amplitude map. The x-axis (α) ranges from the antenna out to half the distance to the Fresnel-Fraunhofer boundary. Note the presence of a second "hotspot" at α = 0.12. Y-axis (τ) ranges over the antenna diameter.

The hotspot seen in Figure 4 ($m \cong 19$) is visible at $\alpha \cong 0.04$, and a second hotspot is now also visible further out-range, centered at $\alpha \cong 0.12$. This second hotspot is weaker ($|E_{H2}| = 1.0$) than the first ($|E_{H1}| = 1.4$), though still significant. In fact, the larger area of the second hotspot increases its effect on average exposure. The locations for these hotspots for the LSSC radars are also listed in Table 1. Due to the large aperture and short wavelength of the Haystack radar, its second hotspot is located 11 km away from the site, furthest of the LSSC radars.

TABLE 1

Near-Field "Hotspots" for the LSSC Radars*

	F_0 (MHz)	Diameter (m)	z_{H1} (km)	z_{H2} (km)	z_{FF} (km)
150' MISA	440	45.7	0.25	0.74	6.1
220' Zenith	440	67.1	0.54	1.6	13.2
Millstone	1,295	25.6	0.23	0.68	5.7
Haystack LRIR†	10,000	37.0	3.7	11.	91.3
HAX	16,700	12.0	0.66	1.9	16.0
HUSIR W-band	96,000	37.0	35.9	105.9	876.7

2.6 NUMERICAL NEAR-FIELD MODEL

Computation of the near-field of an ideal antenna can be performed through integration of its far-field pattern, or plane-wave spectrum. Lewis and Newell [3] note that difficulties arise, however, when the problem is discretized for evaluation on a computer. Special care must be taken to properly sample the spatial frequency domain so that numerical stability is achieved.

The far-field plane wave spectrum $\underline{b}(\underline{K})$ is expressed (using the symbology of the reference) as

$$\underline{b}(\underline{K}) = C\frac{1}{\lambda}e^{-j\gamma d}\int_{-\infty}^{\infty}\int \underline{B}_0(\underline{P})e^{-j\underline{K}\cdot\underline{P}}d\underline{P} \tag{15}$$

where the underscore denotes a vector. $\underline{K}$ is the cartesian spatial frequency vector in the plane of the far-field (where $\underline{K} = k_x\hat{\underline{a}}_x + k_y\hat{\underline{a}}_y$), $\underline{B}_0(\underline{P})$ represents the complex field at cartesian point $\underline{P}$ in a known planar cut of the near-field, λ is the wavelength, $\gamma = \sqrt{k^2 + K^2}$, where $k = 2\pi/\lambda$ and $K^2 = \underline{K}\cdot\underline{K}$, and C is a constant that scales the result for the input power to the antenna. In the reference $\underline{B}_0(\underline{P})$ represents a planar measurement of the near-field on a compact antenna range (a distance d from the aperture), where such a measurement is possible, but is used here to describe the illumination of the aperture itself (i.e., $d = 0$). It can be seen that the form of the relationship between the near-field and the far-field resembles the Fourier Transform and is exploited computationally by the Fast Fourier Transform in the computer implementation.

For the numerical version, a two-dimensional array representing $\underline{B}_0(\underline{P})$ is loaded with equiphase samples of the antenna illumination, accounting for input power and taper. The samples are spaced by no more than $\lambda/2$ for a sufficient Nyquist representation. The array is zero-padded, out to N_x by N_y samples, where

* First hotspot (Z_{H1}) normalized amplitude is approximately 1.4. Second hotspot (Z_{H2}) normalized amplitude is approximately 1.0. Antenna diameters and Fresnel-Fraunhofer boundary distances are also shown.
† Also HUSIR X-band.

$$N_x = N_y \geq 4\sqrt{\frac{Z_{\max}}{\lambda}}, \tag{16}$$

and Z_{max} is the maximum z-distance from the aperture that a near-field representation will be computed for, such that the resulting plane-wave spectrum has sufficient spectral resolution for subsequent operations. A two-dimensional FFT of this array produces the far-field plane-wave spectrum $\underline{b}(\underline{K})$.

Analytic computation of the complex near-field at a point $\underline{r}$ (where $\underline{r} = x\hat{\underline{a}}_x + y\hat{\underline{a}}_y + z\hat{\underline{a}}_z$ as in Figure 3) from the far-field representation is by

$$\begin{aligned} \underline{E}(\underline{r}) &= \frac{1}{2\pi}\int_{-\infty}^{\infty}\int \underline{b}(\underline{K})e^{j\underline{k}\cdot\underline{r}}\,d\underline{K} \\ &= \frac{1}{2\pi}\int e^{jk_x x}\int e^{j\gamma z}\,\underline{b}(\underline{K})e^{jk_y y}\,dk_y\,dk_x, \end{aligned} \tag{17}$$

where $\underline{k} = \underline{K} + \gamma\hat{\underline{a}}_z$. This is performed numerically through an inverse 2D FFT after first performing the $e^{j\gamma z}$ phase shift to the plane-wave spectrum samples as indicated in (17).

In the interest of numerical stability, the plane-wave spectrum is also masked to remove the contribution of small high-frequency components that analytically average out to zero, but numerically can integrate to large values because they are undersampled. The maximum spatial frequency represented must allow for adjacent sample phase change (change in γz) of not more than π. As such, spectrum samples are set to zero when

$$\frac{|k_x| + |k_y|}{k} > \frac{R_0 + D}{\sqrt{R_0^2 + z^2}}, \tag{18}$$

where $R = \pi/\Delta$, Δ is the frequency spacing of the plane-wave spectrum samples, and D is the diameter of the antenna aperture.

The resulting inverse 2D FFT is a cut of the near-field in the x-y plane at a distance z from the aperture. An x-z map of the predicted field similar to that shown for the Pazin model in Figure 5 is shown below in Figure 6. The z-axis is electric field strength for the Millstone L-band radar in V/m.

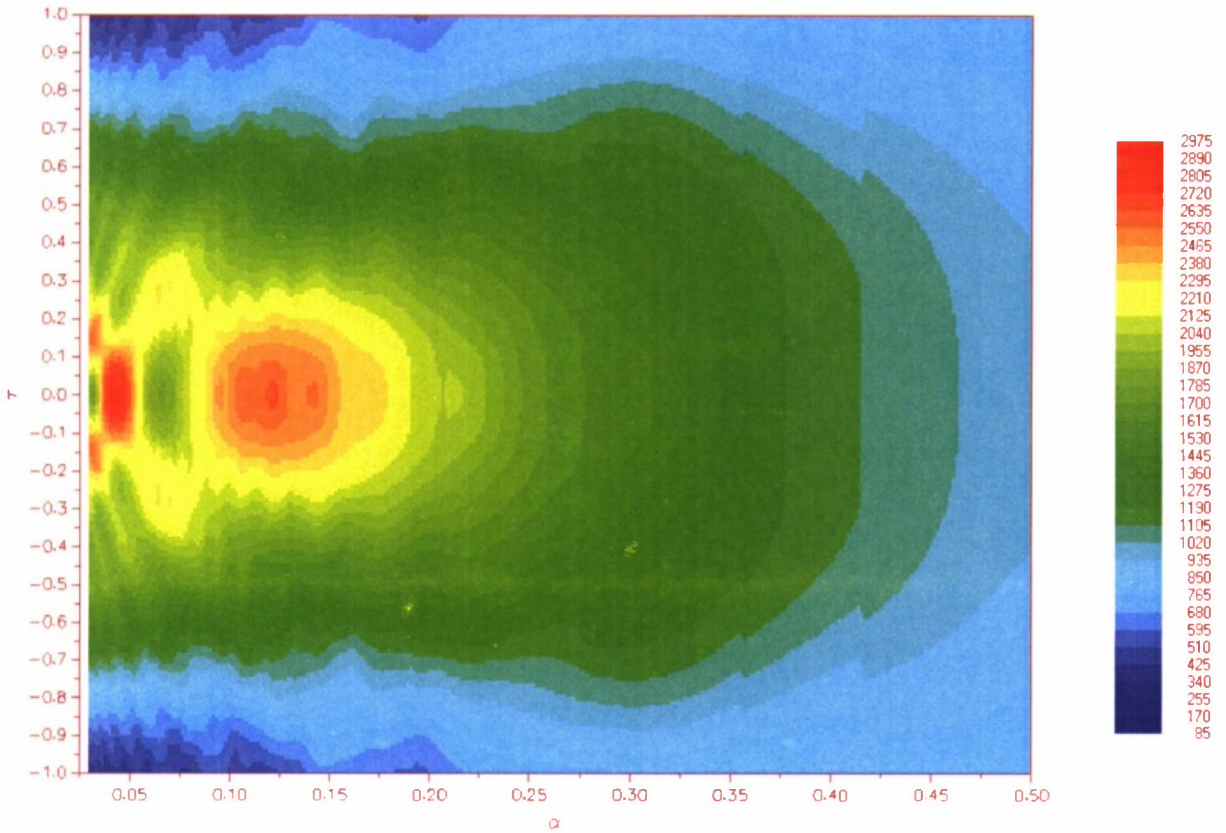

Figure 6. Predicted beam near-field for the Lewis/Newell model. The x-axis (α) ranges from the antenna out to half the distance to the Fresnel-Fraunhofer boundary. Y-axis (τ) ranges over the antenna diameter.

Once the fine adjustments of the Lewis/Newell numerical model are sorted out, it agrees well with the Pazin analytic model, with a less than 1% difference in computed results between the two. For this reason, the results shown in the next section were computed with the Pazin model due to its faster execution speed.

3. RESULTS

Far-field and near-field model results for the fixed-wing aircraft case are now presented, and each for a set of flight scenarios. Far-field results are presented as minimum allowable distances, indicating the minimum RLOS cross-over distances while staying below the state limits based on that model. Near-field results are presented as exposure levels for cross-over distances at the two model hotspots: the worst-case distances. Maximum exposure time maps for near-field results for helicopters are also presented.

Nonionizing radiation limits are established as 30-minute power flux averages. The power flux results presented below are equivalent 30-minute averages, produced by scaling computed average flux levels for the beam transit intervals. The radar system parameters and aircraft flight scenarios used in computation of the results are presented first.

3.1 RADAR SYSTEM PARAMETERS

The system values used in this study are shown in Table 2 for the five systems located at the LSSC. The transmit powers listed are the highest levels used; typical power levels are somewhat lower. The transmit losses are not routinely measured, though the actual values are probably not significantly lower than those shown.

TABLE 2

Radar System Parameters* Used in Analysis of Aircraft RF Radiation Exposure

	F_0 (MHz)	P_X (kW)	Duty (%)	L_X (dB)	G_X (dB)	Beam Size (deg)	1st Sidelobe (dB)
150' MISA	440	2,500	6	0.5	43.5	6	–23
220' Zenith	440	2,500	6	0.5	46.5	4	–21
Millstone	1,295	2,500	4	1	47.1	2	–16
Haystack LRIR‡	10,000	250	30	0.9	68	0.2	<–35
HAX	16,700	50	20	0.7	64	0.4	<–35
HUSIR W-band	96,000	1	40	3.3§	89	0.02	–25

3.2 FIXED-WING AIRCRAFT FLIGHT PARAMETERS

Determining the minimum distance an aircraft has to maintain from a radar depends on its groundspeed and the angle between its flight path and the radar line-of-sight. For the results shown below, two speeds and a number of angles were used.

A groundspeed of 28 ms^{-1} (63 mph) has been chosen to represent the worst case of a single-engine private aircraft near its stall speed, where 45 ms^{-1} (101 mph) represents a more typical speed.

---

* Beam size is defined as the angular distance between the first sidelobes of the antenna far-field radiation pattern. Height of the first sidelobes is relative to the pattern peak (boresight). Loss factors are approximate.

‡ Also HUSIR X-band

§ Includes radome losses

A worst-case flight path angle of 3° has been chosen to represent an aircraft in level flight lined up with the radar azimuth while the radar tracks at its minimum operating elevation of 3°. Angles of 5° and 10° were also chosen as still stressful, but more likely, scenarios. The minimum angle for the 150' MISA far-field results is 6° due to its 6° beam size, and the 60° angle shown for the 220' Zenith system represents an aircraft with a 30° descent angle passing directly over the antenna.

For estimating exposure of birds in flight, groundspeed of 5 ms^{-1} was chosen. This is typical of the slowest avian groundspeeds reported by some observers [4]. The bird exposure levels were estimated using the near-field model only.

3.3 FIXED-WING FAR-FIELD MODEL RESULTS

Results for the flight parameters described above are now presented for the far-field model. Beam transit times and minimum allowable ranges are shown, as are the approximate Fresnel-Fraunhofer boundaries (z_{FF}; see (14)) for comparison. Results are not presented for the HUSIR system due to its extremely distant far-field transition. Note that all the minimum ranges fall well within the z_{FF} boundaries, suggesting this model is not well suited to the situation at hand.

The results are tabulated for two antenna beam representations: the triangular response approximation described above and the numerically estimated antenna pattern beam factor between the first sidelobes of the measured Millstone antenna sum-channel pattern (F_{beam} = 0.31). This measured pattern better approximates the $\sin x/x$-like behavior of a circular aperture.

TABLE 3

MISA UHF System Far-Field Model Transit Time and Minimum Range Results for Various Flight Scenarios

150' MISA	Transit (sec)		Min. Range (m)		z_{FF} (km)
	Triang.	Numeric	Triang.	Numeric	
6° / 28 ms^{-1}	39.08	23.83	820	500	6.1
6° / 45 ms^{-1}	15.12	9.19	510	310	
10° / 28 ms^{-1}	11.59	7.09	490	300	
10° / 45 ms^{-1}	4.56	2.80	310	190	

TABLE 4

Zenith UHF System Far-Field Model Transit Time and Minimum Range Results for Various Flight Scenarios

220' Zenith	Transit (sec)		Min. Range (m)		z_{FF} (km)
	Triang.	Numeric	Triang.	Numeric	
60° / 28 ms^{-1}	0.40	0.23	140	80	13.2
60° / 45 ms^{-1}	0.16	0.09	90	50	

TABLE 5

Millstone L-Band System Far-Field Model Transit Time and Minimum Range Results for Various Flight Scenarios

Millstone	Transit (sec)		Min. Range (m)		z_{FF} (km)
	Triang.	Numeric	Triang.	Numeric	
3° / 28 ms^{-1}	7.23	4.29	270	160	5.7
3° / 45 ms^{-1}	2.83	1.67	170	100	
10° / 28 ms^{-1}	0.58	0.36	80	50	
10° / 45 ms^{-1}	0.23	0.14	50	30	

TABLE 6

Haystack X-Band System Far-Field Model Transit Time and Minimum Range Results for Various Flight Scenarios

Haystack LRIR	Transit (sec)		Min. Range (m)		z_{FF} (km)
	Triang.	Numeric	Triang.	Numeric	
3° / 28 ms^{-1}	4.84	2.96	2030	1240	91.3
3° / 45 ms^{-1}	1.88	1.14	1270	770	
10° / 28 ms^{-1}	0.45	0.27	620	380	
10° / 45 ms^{-1}	0.17	0.11	390	240	

TABLE 7

HAX K_u-Band System Far-Field Model Transit Time and Minimum Range Results for Various Flight Scenarios

HAX	Transit (sec)		Min. Range (m)		z_{FF} (km)
	Triang.	Numeric	Triang.	Numeric	
3° / 28 ms^{-1}	1.10	0.67	230	140	16.0
3° / 45 ms^{-1}	0.45	0.27	150	90	
10° / 28 ms^{-1}	0.10	0.07	70	50	
10° / 45 ms^{-1}	0.04	0.03	50	30	

3.4 FIXED-WING NEAR-FIELD MODEL RESULTS

Results for the flight parameters described above are now presented for the near-field model. Worst-case exposure levels for flights through the two hotspots (denoted H1 and H2), the positions of which are tabulated in Table 1, are shown. The field strength limit established by the Mass. Dept. of Public Health [5], which is a function of radiation frequency, is also shown. Quoted exposure levels are average power fluxes for a 30-minute period, as specified by the state standard.

TABLE 8

MISA UHF System Near-Field Model Results for Various Flight Scenarios*

150' MISA	Exposure (mW/cm^2)		Limit (mW/cm^2)
	H1	H2	
3° / 28 ms^{-1}	0.27	0.25	0.293
3° / 45 ms^{-1}	0.17	0.15	
5° / 28 ms^{-1}	0.16	0.15	
5° / 45 ms^{-1}	0.10	0.09	
6° / 28 ms^{-1}	0.13	0.12	
6° / 45 ms^{-1}	0.083	0.077	
10° / 28 ms^{-1}	0.080	0.074	
10° / 45 ms^{-1}	0.050	0.046	

TABLE 9

Zenith UHF System Near-Field Model Results for Various Flight Scenarios*

220' Zenith	Exposure (mW/cm^2)		Limit (mW/cm^2)
	H1	H2	
60° / 28 ms^{-1}	0.011	0.010	0.293
60° / 45 ms^{-1}	0.007	0.006	

* Computed exposure is equivalent 30-minute average power flux for beam transit through field hotspot H1 or H2.

TABLE 10

Millstone L-Band System Near-Field Model Results for Various Flight Scenarios*

Millstone	Exposure (mW/cm^2)		Limit (mW/cm^2)
	H1	H2	
3° / 28 ms^{-1}	0.33	0.31	0.863
3° / 45 ms^{-1}	0.21	0.19	
5° / 28 ms^{-1}	0.20	0.18	
5° / 45 ms^{-1}	0.12	0.11	
10° / 28 ms^{-1}	0.098	0.092	
10° / 45 ms^{-1}	0.061	0.057	

TABLE 11

Haystack X-Band System Near-Field Model Results for Various Flight Scenarios*

Haystack LRIR	Exposure (mW/cm^2)		Limit (mW/cm^2)
	H1	H2	
3° / 28 ms^{-1}	0.16	0.15	1.000
3° / 45 ms^{-1}	0.10	0.095	
5° / 28 ms^{-1}	0.098	0.092	
5° / 45 ms^{-1}	0.061	0.057	
10° / 28 ms^{-1}	0.049	0.046	
10° / 45 ms^{-1}	0.031	0.029	

TABLE 12

HAX K_u-Band System Near-Field Model Results for Various Flight Scenarios*

HAX	Exposure (mW/cm^2)		Limit (mW/cm^2)
	H1	H2	
3° / 28 ms^{-1}	0.067	0.063	1.000
3° / 45 ms^{-1}	0.042	0.039	
10° / 28 ms^{-1}	0.020	0.019	
10° / 45 ms^{-1}	0.013	0.012	

* Computed exposure is equivalent 30-minute average power flux for beam transit through field hotspot H1 or H2.

TABLE 13

HUSIR W-Band System Near-Field Model Results for Various Flight Scenarios*

HAX	Exposure (mW/cm^2)		Limit (mW/cm^2)
	H1	H2	
3° / 28 ms^{-1}	<0.001	<0.001	1.000
3° / 45 ms^{-1}	<0.001	<0.001	
10° / 28 ms^{-1}	<0.001	<0.001	
10° / 45 ms^{-1}	<0.001	<0.001	

Though the amplitude of the second hotspot (H2) is lower than the first (H1), its broader extent causes the exposure levels to be close to those encountered at H1.

For the 1 kW HUSIR W-band transmitter, the H1 peak power density is only 0.486 mW/cm^2. The average power density with 40% duty cycle is 0.194 mW/cm^2. The exposure limit at W-band for general population is 1 mW/cm^2, so the W-band beam exposure is safe for an unlimited amount of time. Exposure for all fixed-wing flight scenarios is less than 0.001 mW/cm^2.

HUSIR will be a dual-band radar, with X-band and W-band beams co-boresighted and radiating simultaneously, so a cumulative X- and W-band exposure could be a concern. However, in W-band, the H1 hotspot is at 36 km, or 25 km beyond the X-band H2 hotspot. Since the X-band and W-band hotspots are so widely separated, there is no significant cumulative effect.

Note that under even these unlikely flight conditions, an aircraft transiting the beam is not exposed to RF radiation that exceeds the state maximum limit. The only case that is close is where the aircraft is almost stalling and traveling only 3° off boresight of the MISA UHF radar (see Table 8).

A similar model can be applied to calculate the exposure level for birds flying through the HUSIR beam. The primary concern here is the X-band radar beam due to its much higher power density (H1 average power density is approximately 40 mW/cm^2). Table 14 summarizes the results.

TABLE 14

HUSIR X-Band System Near-Field Model Results for Bird Flight Scenarios*

Haystack LRIR	Exposure (mW/cm^2)	
	H1	H2
3° / 5 ms^{-1}	0.9	0.8
5° / 5 ms^{-1}	0.5	0.5
10° / 5 ms^{-1}	0.3	0.3

* Computed exposure is equivalent 30-minute average power flux for beam transit through field hotspot H1 or H2.

While the exposures in Table 14 are below the allowable limits for genral human population, the Commonwealth ef Massaehusetts does not speeify safe exposures for birds. However, Bruederer, Peter, and Steuri [6] studied the effeets of tracking birds with X-band (9 GHz) radar on their behavior. The average power densities of their radar beam ranged from 40 mW/em^2 at 250 meters to 2.5 mW/em^2 at 1,000 meters. Birds were traeked for a minimum of 60 see and no ehanges in behaviour were observed. These results imply that there is no signifieant effeet on birds from short duration exposures to RF radiation at these power densities. As in the aireraft seenarios, the flight geometries used in Table 12 are extreme. Most exposures due to birds aeeidentally erossing the beam are expeeted to be at higher angles and, thus, of mueh shorter duration. Table 15 summarizes the exposure times to various RF power density levels for birds erossing the radar boresight at a more typieal 45 degree angle and 5 ms^{-1} air speed. The MISA UHF radar is the worst ease due to its large beam width. For this seenario (45 deg, 5 ms^{-1}), the 30 minute average power density for a bird erossing any LSSC radar beam is less than 1 mW/em^2.

TABLE 15

Summary of RF Exposure Times to Birds Crossing the Radar Boresight at 45 Degree Angle and 5 ms^{-1} Air Speed

Average Power Density Level (mW/cm^2)	Exposure Time (sec) for MISA UHF	Exposure Time (sec) for HUSIR X-Band	Exposure Time for HUSIR W-Band
>100 mW/cm^2	0	0	0
>10 mW/cm^2	14	6	0
>1 mW/cm^2	21	11	0

3.5 HELICOPTER NEAR-FIELD MODEL RESULTS

After studying the near-field models, it quickly beeomes apparent that the only place where the field is signifieantly strong is within the near-field beam itself, whieh is to say within one antenna aperture radius of the radar line-of-sight. For the helieopter ease, where the aireraft ean hover and dwell at a partieular loeation for many minutes, the best way to visualize the problem is by eomputing the maximum amount of time the helieopter ean stay at a fixed position in the beam before the exposure exeeeds the maximum limit. This maximum dwell time assumes neither the aireraft nor the radar antenna moves during the eneounter.

Shown below (Figures 7–11) are x-z maps of the near-fields of the LSSC radars indieating the maximum time a helieopter may dwell at a partieular position.

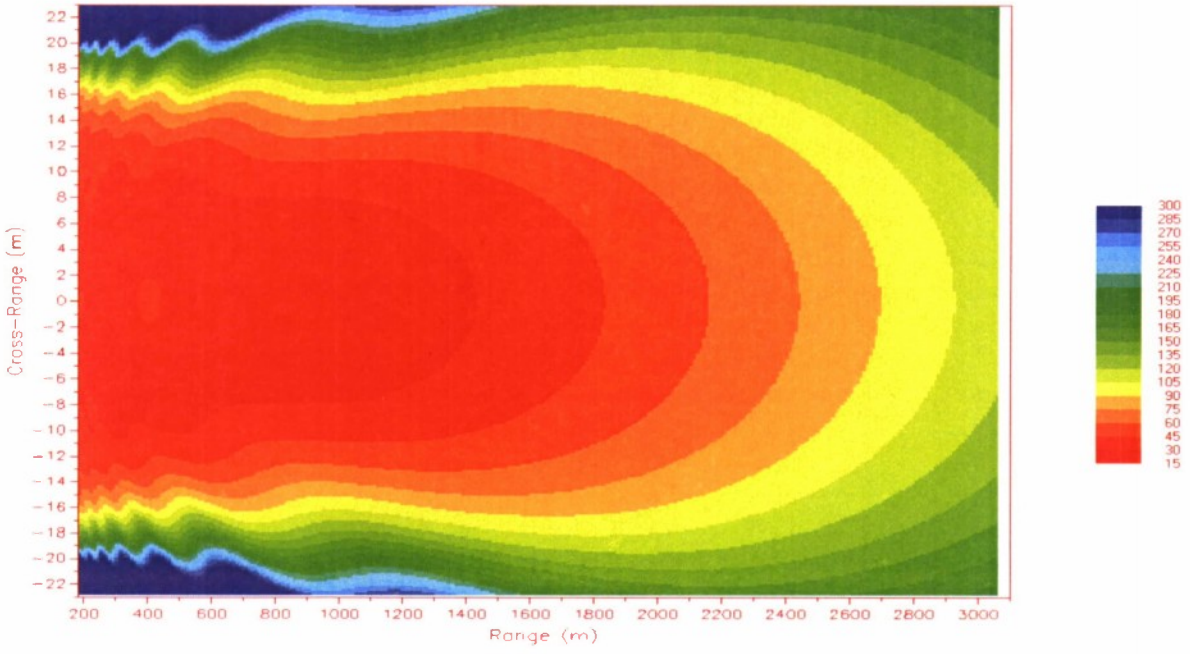

Figure 7. MISA UHF system map of maximum allowable exposure times for a hovering helicopter. X-axis is range from radar antenna aperture, y-axis is cross-range spanning the diameter of the aperture, and z-axis is seconds of dwell time.

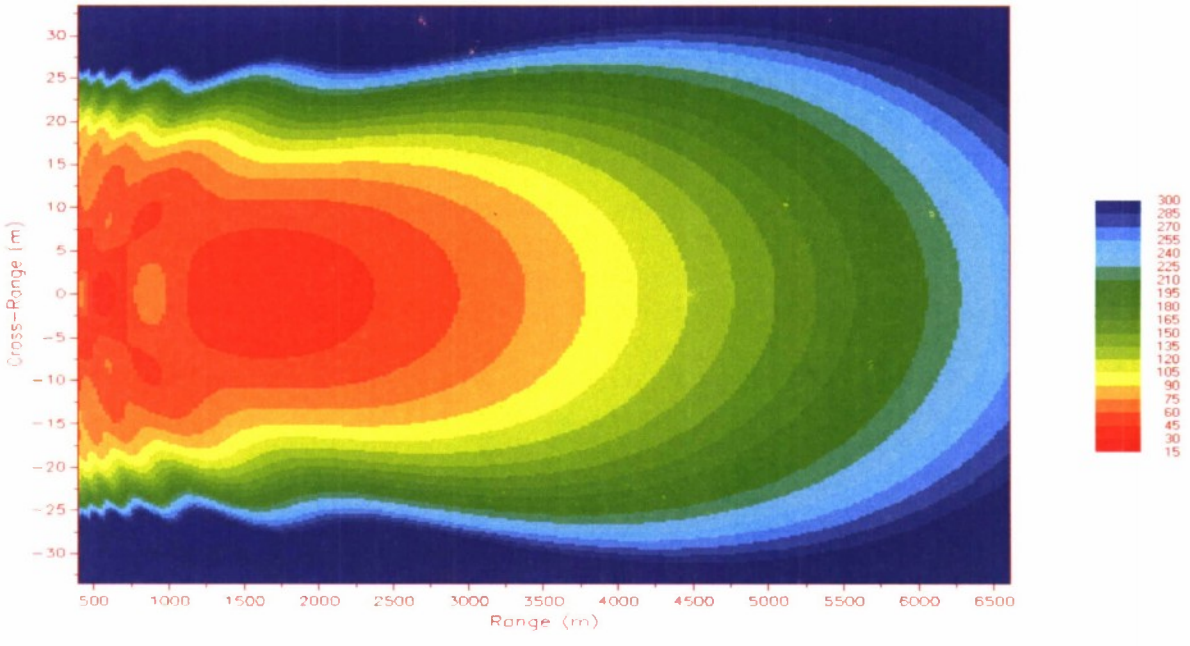

Figure 8. Zenith UHF system map of maximum allowable exposure times for a hovering helicopter. X-axis is range from radar antenna aperture, y-axis is cross-range spanning the diameter of the aperture, and z-axis is seconds of dwell time.

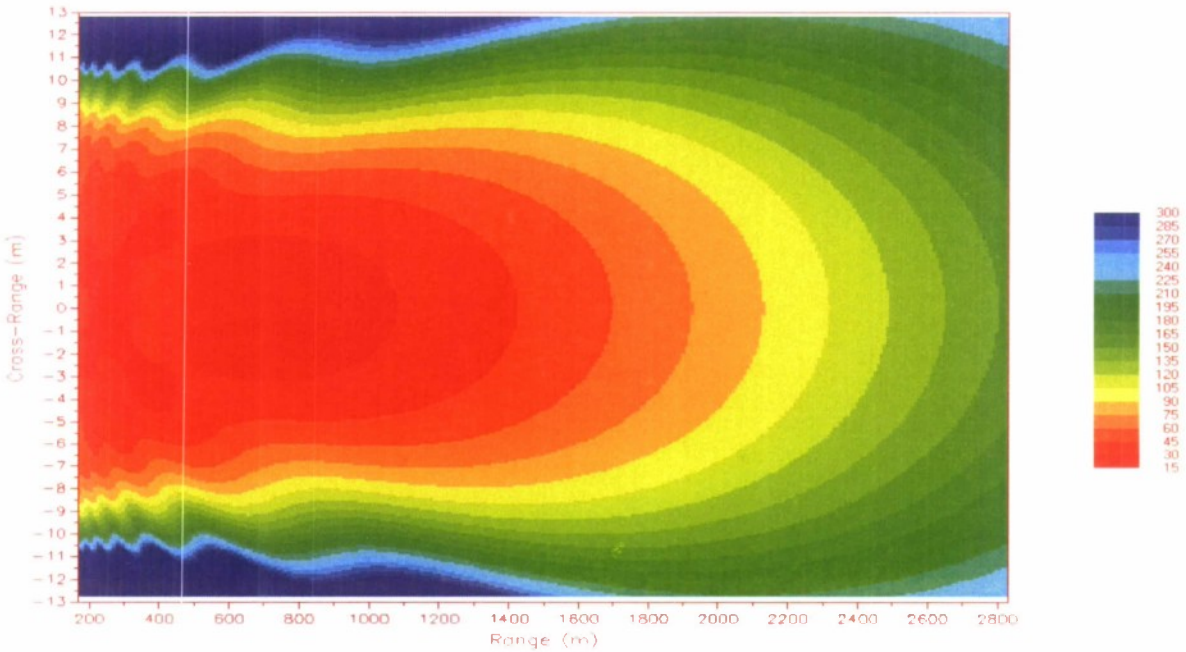

Figure 9. Millstone L-band system map of maximum allowable exposure times for a hovering helicopter. X-axis is range from radar antenna aperture, y-axis is cross-range spanning the diameter of the aperture, and z-axis is seconds of dwell time.

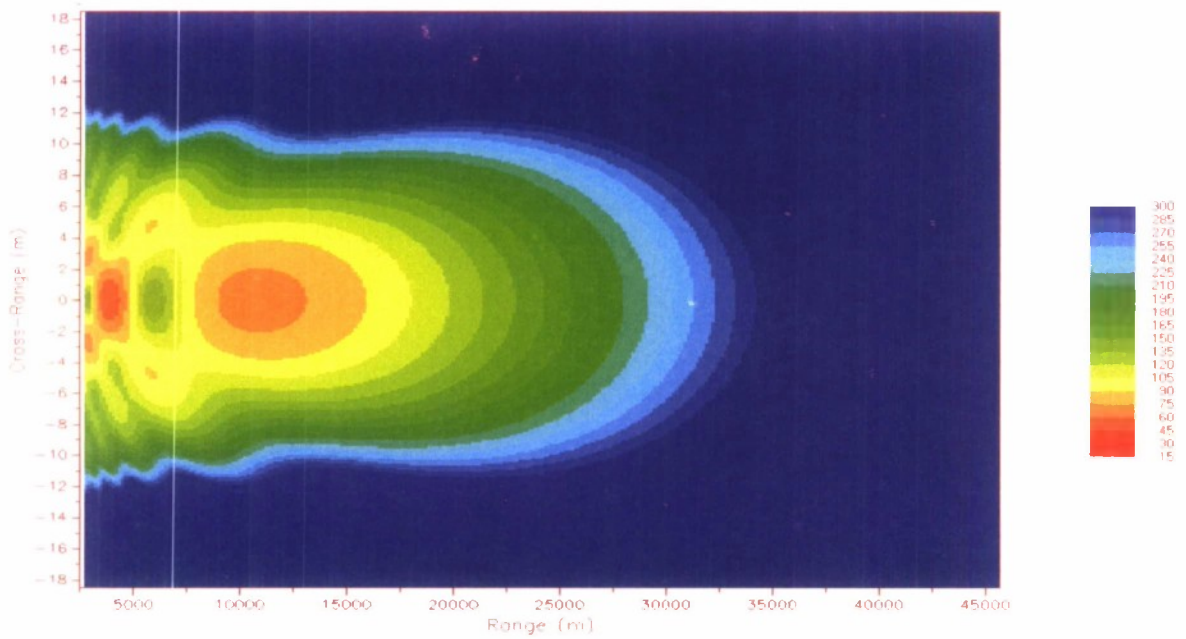

Figure 10. Haystack X-band system map of maximum allowable exposure times for a hovering helicopter. X-axis is range from radar antenna aperture, y-axis is cross-range spanning the diameter of the aperture, and z-axis is seconds of dwell time.

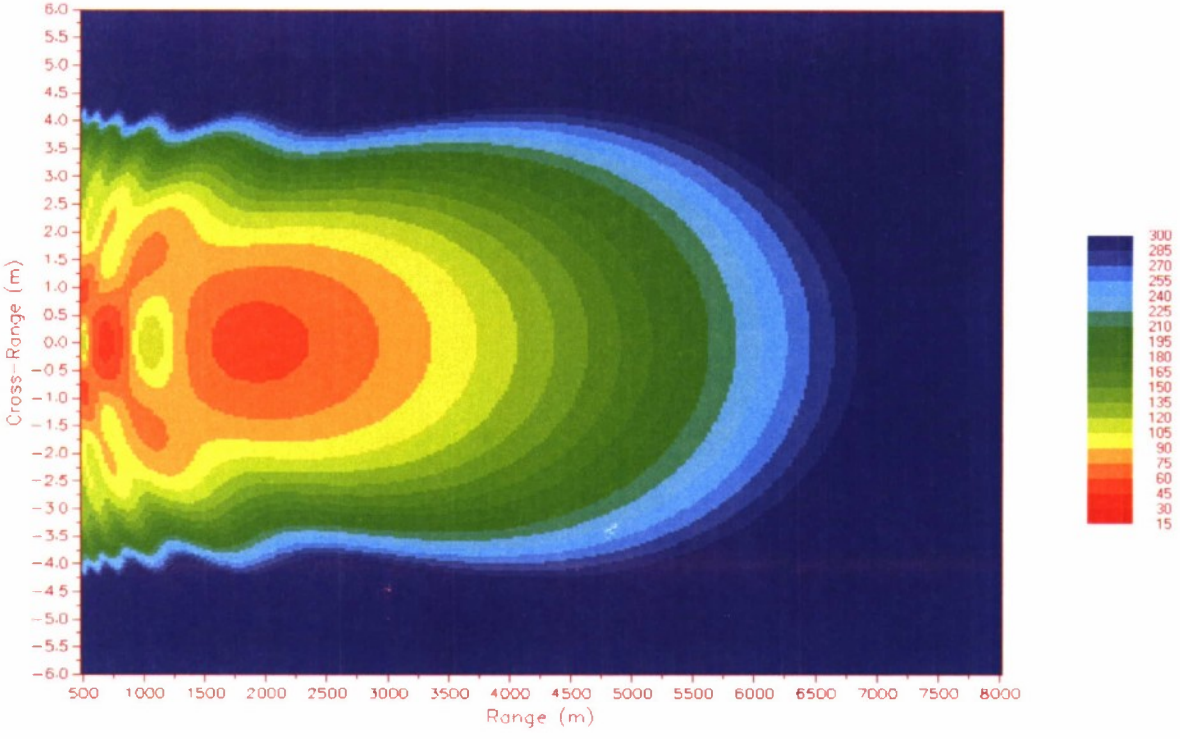

Figure 11. HAX K_u-band system map of maximum allowable exposure times for a hovering helicopter. X-axis is range from radar antenna aperture, y-axis is cross-range spanning the diameter of the aperture, and z-axis is seconds of dwell time.

As can be seen, a helieopter must be within the eylinder of the antenna aperture before the risk of over-exposure is signifieant. Further, for the higher-frequeney radars, Haystaek LRIR and HAX, the aireraft must be within only a few meters of boresight. In all eases, onee the helieopter is outside of the near-field beam, it may hover for five minutes and more without reaching the maximum limit. Due to the narrow beams of these radar systems, the exposure to objeets outside of the beam is low.

As shown in Figure 12, the HUSIR W-band peak power flux density is below the Commonwealth of Massachusetts exposure limit for general population, so a helieopter can stay in any part of the W-band beam indefinitely. Due to the relatively low power of the W-band transmitter, the results for HUSIR eumulative exposure (X- and W-bands simultaneously) are essentially identieal to Haystaek LRIR (X-band only).

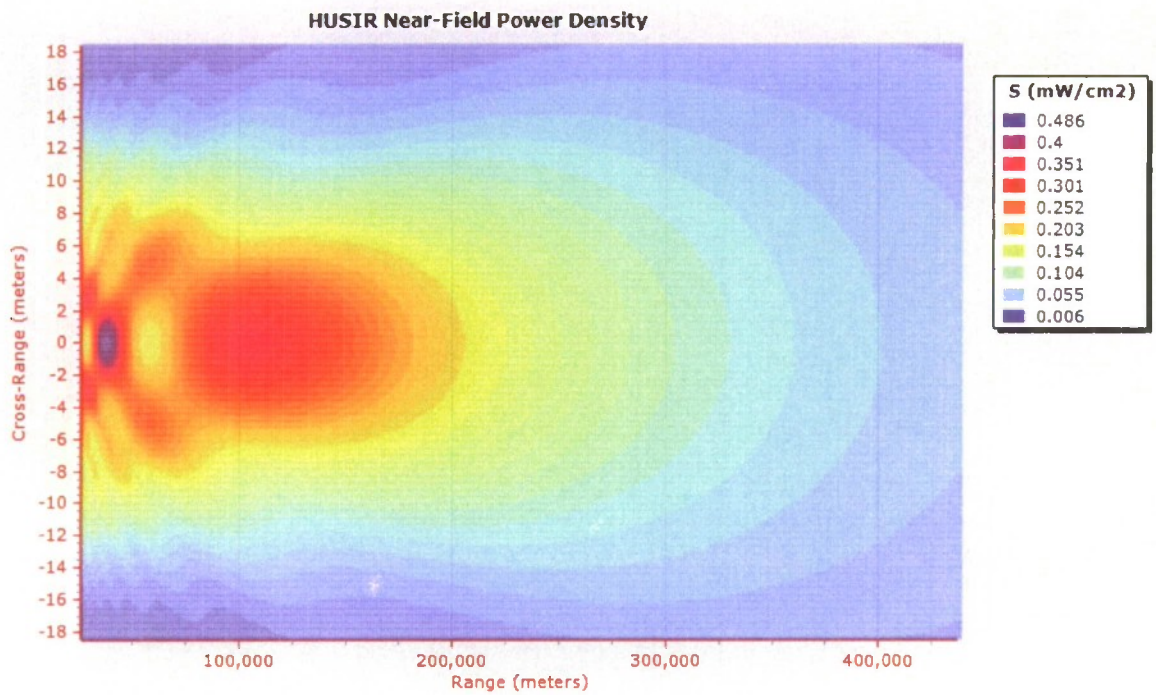

Figure 12. HUSIR W-band near-field power flux density map. X-axis is range from radar antenna aperture, y-axis is cross-range spanning the diameter of the aperture, and z-axis is peak power flux density in mW/cm^2. Since the maximum duty cycle of the W-band radar is 40%, these values need to be multiplied by 0.4 to obtain the average power flux density.

This page intentionally left blank.

4. CONCLUSIONS

The RF radiation exposure levels to fixed-wing aircraft, rotary-wing aircraft, and birds have been studied. The selected near-field model, necessary for the close ranges in question, has been corroborated. Results from the addition of the HUSIR radar system have been shown along with earlier findings for all of the other LSSC radar systems. Both likely and unlikely scenarios for the anticipated operations of the Millstone Hill radar systems have been included. Even though the potential for main-beam thermal effects exposure exists for these special-purpose, high-power, deep-space radar systems, the beam size, pulsed/high-speed scanning operational scenarios reduce the likely exposure to airborne aircraft to levels that are extremely small and that are below the Massachusetts and FCC exposure limits for the general public. While there are no well established exposure limits for birds, studies such as [6] indicate that birds accidentally crossing the Haystack or HUSIR beam will not be affected.

The likelihood of exposure of helicopters to RF levels above the state and federal exposure limits, while still very small, is greater than to fixed-wing aircraft due to their ability to hover and dwell. If a helicopter were to dwell very close to the middle of the beam of any of the LSSC radars, it may be exposed to levels exceeding the maximum limit in under 90 seconds, depending on the distance from the antenna and the proximity to the radar line-of-sight. Based on the result for the MISA radar, a minimum safe distance of 3000 or 3500 meters may be appropriate, though the likelihood of a helicopter pilot positioning himself directly in front of an antenna at that range is not great. For Haystack LRIR, HUSIR, and HAX, the distances are much greater, though the likelihood of positioning within a few meters of boresight is very small, particularly given the curiosity element is not present due to the radomes covering these antennas.

To give an idea of the extent of the distances mentioned above, Figure 13 shows a map of the area around Millstone Hill. A circle of radius 3500 meters (11,550 feet, or almost 2¼ miles) is shown, centered on Haystack. Pilots often use the large radome of the LRIR as a visual reference, so any potential alert zone should be centered there. The distance from Haystack to Millstone is approximately 690 m, and Haystack to the MISA antenna is approximately 480 m. If a 3500 meter radius and a 5° beam elevation is considered, the beam altitude at 3500 meters is approximately 300 meters (1000 feet) above Haystack ground level, or 425 meters (1400 feet) above mean sea level.

As shown in Table 15, the potential for main-beam short duration exposure to birds exists. The results indicate that only the UHF radars may present a small risk to birds of thermal effects due to exposure to RF power densities greater than 10 mW/cm^2 (less than 14 seconds exposure for birds crossing the radar boresight at 45 degrees) with all other exposures significantly lower.

The analysis summarized in this report shows that there is a very low probability of impact on fixed-wing and rotary-wing aircraft, migrating birds as well as resident bird populations.

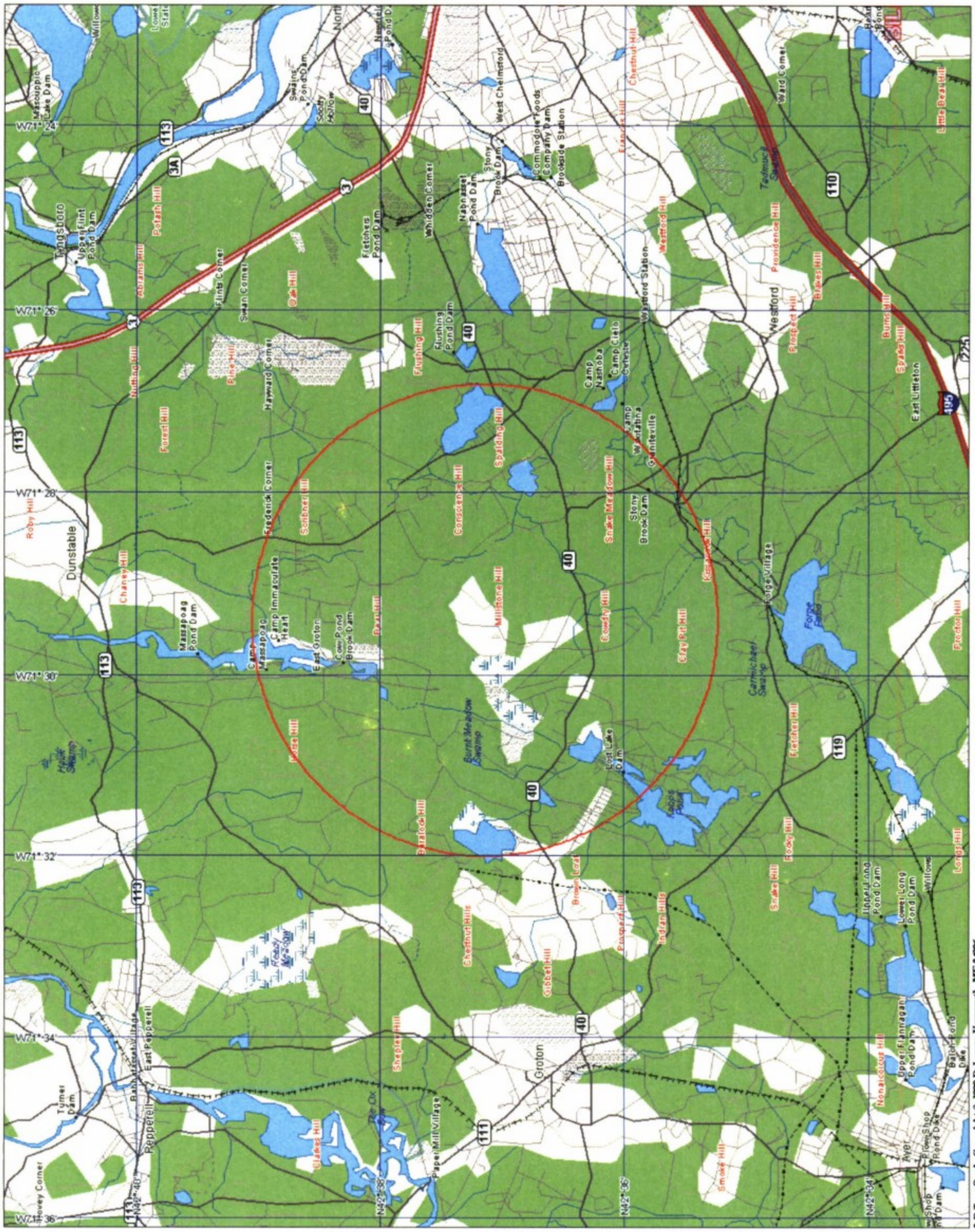

Figure 13. Map of the area around Millstone Hill. The red circle, centered at Haystack, has a radius of approximately 3500 m.

REFERENCES

1. D. Slater, *Near-Field Antenna Measurements*, Artech House (1991).

2. L.Z. Pazin, "Field of a Circular Aperture Antenna in the Fresnel Diffraction Region," *Journal of Communications Technology and Electronics,* Vol. 41, No. 15, 1347–1349 (1996). Translated from *Radiotekhnika I Elektronika*, Vol. 41, No. 12, 1468–1470 (1996).

3. R. L. Lewis and A. C. Newell, "Efficient and Accurate Method for Calculating and Representing Power Density in the Near Zone of Microwave Antennas," *IEEE Transactions on Antennas and Propagation*, Vol. 36, No. 6, 890–901 (1988).

4. S. Kleinhaus *et al.*, "Thermal Effects of Short Radio Waves on Migrating Birds," *Ecological Applications*, Vol. 5, No. 3, 672–679 (1995).

5. Massachusetts Department of Public Health document 105 CMR, Section 122.015, Table 1 "Non-occupational Radiofrequency Exposure Limits for the General Public" (1997).

6. B. Bruderer, D. Peter, and T. Steuri, "Behaviour of Migrating Birds Exposed to X-band Radar and a Bright Light Beam," *The Journal of Experimental Biology*, Vol. 202, 1015–1022 (1999).

This page intentionally left blank.

REPORT DOCUMENTATION PAGE

Form Approved
OMB No. 0704-0188

1. REPORT DATE	2. REPORT TYPE	3. DATES COVERED *(From - To)*
14 December 2009	Technical Report	

4. TITLE AND SUBTITLE

RF Radiation Environment Over Millstone Hill

5a. CONTRACT NUMBER
FA8721-05-C-0002

5b. GRANT NUMBER

5c. PROGRAM ELEMENT NUMBER

6. AUTHOR(S)

T. Andrew Cott, Group 93

5d. PROJECT NUMBER
1247

5e. TASK NUMBER
114

5f. WORK UNIT NUMBER

7. PERFORMING ORGANIZATION NAME(S) AND ADDRESS(ES) AND ADDRESS(ES)

MIT Lincoln Laboratory
244 Wood Street
Lexington, MA 02420-9108

8. PERFORMING ORGANIZATION REPORT NUMBER
TR-1141

9. SPONSORING / MONITORING AGENCY NAME(S) AND ADDRESS(ES)

830 ELSG/NSS
11 Barksdale Street, Bldg. 1614 (Phase 2)
Hanscom AFB, MA 01731-1700

10. SPONSOR/MONITOR'S ACRONYM(S)

11. SPONSOR/MONITOR'S REPORT NUMBER(S)
ESC-TR-2007-082

12. DISTRIBUTION / AVAILABILITY STATEMENT

Approved for public release; distribution is unlimited.

13. SUPPLEMENTARY NOTES

14. ABSTRACT

This report documents a study of the RF radiation environment in the vicinity of the Lincoln Space Surveillance Complex radars. The focus of the study is a model-based analysis of the hazards to occupants of aircraft flying in the vicinity of the radars, comparing computed exposure levels with safety standards for the general public set by the Massachusetts Department of Public Health.

15. SUBJECT TERMS

16. SECURITY CLASSIFICATION OF:			17. LIMITATION OF ABSTRACT	18. NUMBER OF PAGES	19a. NAME OF RESPONSIBLE PERSON
a. REPORT	b. ABSTRACT	c. THIS PAGE			19b. TELEPHONE NUMBER *(include area code)*
Unclassified	Unclassified	Unclassified	Same as report	42	

This page intentionally left blank.